On the Synchronization of Parallel Power Converters via Emulation of Linear Mechanical Oscillators

Matteo Dalboni and Alessandro Soldati, *Member, IEEE*

***Abstract*—There exist some modular mechanical systems that exhibit inherent synchronization capabilities. Among these, arrays of pendula connected to the same moving platform, under some particular conditions that are analyzed in this work, tend to approach the synchronous in-phase or antiphase motion. Such an appealing behavior can be replicated within modular electronic circuits equipped with multiple power converters to achieve the coordination of all units. The approach consists in recasting the mechanical equations of motion of interconnected pendula to the equivalent electrical circuit by impedance or mobility analogy. This allows obtaining a self-synchronizing network without the need of explicit communication between the modules. The effectiveness of the proposed distributed controller is assessed through experimental tests. Therefore, the fundamental points of novelty are the derivation of two (series and parallel) self-synchronizing electrical linear circuits through analogy with mechanical models and the introduction of a distributed voltage-source controller for parallel operation of converters based on a fully linear model. The proposed methodology is effective for both parallel-output converters with independent inputs (as in microgrid applications) and parallel-input and parallel-output converters (as in high-current applications).**

***Index Terms*—Linear oscillator, power converter control, self-synchronization, series-distributed controller, voltage-source converter.**

I. Introduction

IN THE field of mechanics and dynamics, pendula have been studied extensively across many different configurations. By way of example, these oscillators can be involved in the design of active balancing controllers and energy harvesters or in the assessment of numerical solver stability. A number of works focused on the synchronization ability of coupled pendula arranged in parallel, many of them inspired by the original Huygens' observations on mutually coupled clocks [1], [2], [3], and by the well-known experiment that displays how metronomes are prone to synchronize when placed on a common mobile platform [4].

Moving from the mechanical to the power electronics realm, modular converters represent an interesting solution to the necessity to size a power system (e.g., the powertrain of an electric vehicle or a microgrid) based on customer's requirements without the need to design it every time from scratch or to increase its reliability by taking advantage of the redundancy, which translates to multiple points of failure and so continuity of operation.

When voltage-based grids are considered, the modularity is achieved chiefly by parallel operation of voltage-source converters (e.g., inverters in case of ac grids). Parallel converter topologies can be classified in isolated or nonisolated depending on the existence of a direct current path between the input and the output. Nonisolated parallel converters are most commonly used in grid-related applications; for example, isolation is mandatory in medium-voltage ac, i.e. MVac to low-voltage dc (LVdc) conversion, where the converter outputs are connected in parallel, but the inputs are connected in series, which makes the isolation indispensable [5], [6], [7], [8], [9], [10]. Also, the isolation can be achieved at the back end (dc/dc) or at the front end (ac/ac) [8]. Parallel conversion occurs also in isolated fashion in solid-state transformers' applications where multiple ac/dc/ac conversions occur by paralleling on both ac input and ac output. The transformer used to step-up or down the voltage also provides the isolation [11]. However, nonisolated parallel input and parallel output can be used to boost current in drive applications [12]. Anyway, the approach presented in the rest of this article is independent of the isolation among the units since it models the ac generators only at the point of common coupling with the load.

In order to be effective and efficient, a parallel layout requires the synchronization of all of its units. The goal can be achieved by means of proportional–integral (PI) regulators as in [13] for the parallel operation of redundant uninterruptible power supplies. A quite unique synchronization method for parallel converters also based on PI regulator is proposed by

Manuscript received 2 November 2022; revised 18 May 2023; accepted 29 June 2023. Recommended by Technical Editor J. Hey and Senior Editor H. Gao. This work was supported in part by the Programme "FIL-Quota Incentivante" (REBASED) of University of Parma and cosponsored by Fondazione Cariparma, and in part by the National Recovery and Resilience Plan (NRRP), Mission 4 Component 2 Investment 1.5 - Call for tender No. 3277 of 30/12/2021 of MUR funded by the European Union - NextGenerationEU under Project ECS00000033, CUP D93C22000460001, and Project title "Ecosystem for Sustainable Transition in Emilia-Romagna." *(Corresponding author: Matteo Dalboni.)*

The authors are with the Department of Engineering and Architecture, University of Parma, 43124 Parma, Italy (e-mail: matteo.dalboni@unipr.it; alessandro.soldati@unipr.it).

Color versions of one or more figures in this article are available at https://doi.org/10.1109/TMECH.2023.3292534.

Digital Object Identifier 10.1109/TMECH.2023.3292534

Soldati et al. [14]: The distributed control operates directly at pulsewidth-modulation (PWM) level and allows minimizing the circulating current even without filter inductors by relying on the natural parasitic inductance of each converter.

Probably, the most famous distributed method utilized for the sake of parallel functioning of power converters is droop control [15], [16]. However, droop control has some stability issues and exhibits a slow dynamic response: these drawbacks are addressed in [17], where the authors propose a controller consisting of a synchronous-reference-frame virtual impedance loop, a phase-locked loop (PLL), and a proportional–resonant regulator.

A radically different approach consists in designing a circuit endowed with inherent sympathy for the synchronicity. Indeed, some studies report the application of nonlinear electric oscillators to achieve the spontaneous synchronization of parallel electronic converters. Among these, the authors in [18], [19], [20], [21], and [22] present and thoroughly analyze the so-called virtual oscillator control (VOC), which mimics a dead-zone oscillator or an oscillator based on the van-der-Pol law within a digital controller, thus obtaining the synchronicity of coupled single- and three-phase inverters. The substantial advantages of VOC with respect to droop control are also pointed out in [22], while the mathematical relation between the two strategies is delineated in [23]. Similarly, the authors in [24] and [25] achieve the coordination of paralleled dc/ac converters by the Andronov–Hopf virtual oscillator. Other authors proved the analogy between some electronic networks [26], [27] or islanded microgrids [28], and the eminent Kuramoto model [29], thus providing conditions for the synchronized mode and its stability. Another relevant synchronization approach for inverter-based power grids is analyzed by the authors in [30] and [31]. Specifically, the nonlinear control is inspired by consensus strategies, and it ensures almost global asymptotic stability in terms of phase shift, frequency, and magnitude tracking.

The distinctive approach that is proposed in the present investigation consists in synthesizing a couple of self-synchronizing modular circuits by projecting a mechanical linear system made of parallel-connected pendula into the electrical domain. The two modular topologies so obtained are made exclusively of linear components; hence, they can be studied by the well-established theory on linear systems. Also, to the best of the authors' knowledge, the article presented in [32] is the only study available in the literature concerning a circuit made of *series-connected* units capable to spontaneously synchronize without resorting to a communication network; however, the proposed controller emulates a nonlinear oscillator rather than a linear one as that presented in the following of our research. Furthermore, another point of novelty of the present investigation is the design of a distributed voltage-source controller through the emulation of the electrical circuit suitable for the communicationless synchronization of parallel-connected inverters.

Briefly, the key contributions of this study are as follows:

1) derivation of a *series* resonant self-synchronizing circuit, making use of the impedance analogy, and experimental validation of such a circuit;
2) derivation of a *parallel* resonant self-synchronizing circuit, making use of the mobility analogy, and experimental validation of such a circuit;
3) design and experimental validation of a distributed voltage-source controller based on the parallel circuit previously identified; this controller allows the communicationless synchronization of parallel-connected single- and three-phase inverters.

Table I summarizes the fundamental features of the synchronization methods available in the literature and compares them with the novel strategy.

The rest of this article is organized as follows. In Section II, the relevant mechanical models are derived taking inspiration from the system that is generally adopted to study the synchronization of interconnected metronomes. Section III goes through the analysis of the mechanical models, setting the scene for the electrical parallelism. In Section IV, a *series* resonant self-synchronizing circuit is derived, making use of the impedance analogy, and experimentally validated. Similarly, in Section V, a *parallel* resonant self-synchronizing circuit is obtained via the mobility analogy and assessed in the real world. Section VI deals with the design and validation of a voltage-source controller based on the topology identified in Section V. Finally, Section VII concludes this article.

II. Equations of Motion of Parallel Pendula

This section deals with the mathematical background regarding self-synchronizing mechanical systems.

The first model (referred to as *Model A* in the following) is inspired by Dilao [3], and it can be regarded as a generalization of the nonlinear models that are often proposed to study arrays of metronomes (see [2], [4]). The second model that is analyzed (henceforth referred to as *Model B*) can be considered as a simplified version of the former: Model *B* is linear, conservative in steady state, and, consequently, well suited for the electrical analogy.

Both mechanical models comprise a base and pendula. Throughout this article, the quantities related to the former are denoted by the subscript b, whereas those connected to the latter are indicated by the subscript p. The same nomenclature convention is adopted also in the analysis of the analogous electrical models to emphasize how each component is related to the original mechanical systems.

A. Pendula on Flexible Base (Model A)

This system includes n pendula; its base is decomposed into as many lumped masses as the pendula are, and such bodies are interconnected by springs and dampers (see Fig. 1). The coordinates of the center of mass of the pendulum j are

$$x_{p_j} = x_{b_j} + l \sin \theta_j \tag{1a}$$

$$y_{p_j} = -l \cos \theta_j \tag{1b}$$

where θ_j is the angle that the pendulum j defines with the vertical, and l is the pendulum length. Also, the horizontal

TABLE I
COMMUNICATIONLESS SYNCHRONIZATION METHODS FOR PARALLEL-CONNECTED CONVERTERS

Method	Pros	Cons
Voltage drop compensator [13]	• Simple implementation • Uneven load sharing	• Slow dynamics since it operates on averaged phasors (phasor-domain strategy)
Double edge sampler [14]	• It operates at PWM level • No filters needed	• It can compensate only phase mismatches
Droop control [15], [16]	• Well-established • Uneven load sharing	• Slow dynamics since it operates on averaged phasors (phasor-domain strategy)
Synchronous-reference-frame virtual impedance loop with PLL [17]	• Faster than droop control	• Limited bandwidth due to PLL • Complex design of virtual impedance • Stability issues
Virtual oscillator control (VOC) [18]–[23]	• Fast dynamics (time-domain strategy) • Independence from loads • Uneven load sharing	• Initial conditions affect its stability • Signal distortion with inadequate parameters • Not well suited for three-phase systems • Analysis can be complicated due to nonlinearity
Andronov-Hopf VOC (AHO) [24], [25]	• Simpler, faster and more robust than VOC	• Coupling effect of active and reactive power
Dispatchable VOC (dVOC) [30], [31]	• Almost global asymptotic stability	• Coupling effect of active and reactive power
Proposed method	• Conceived for general-purpose modular applications • Time-domain strategy • Simple analysis and tuning • Suitable for single- and three-phase inverters	• Additional loop required for voltage (or current) amplitude regulation • Uneven load sharing still unexplored • Active and reactive power control still unexplored

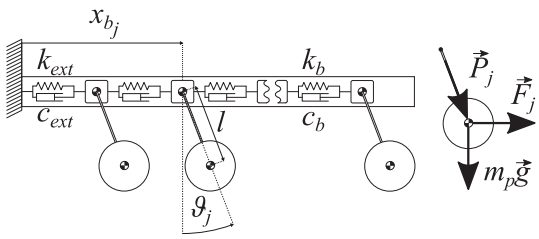

Fig. 1. Schematic of pendula on flexible base (Model *A*) and free-body diagram of the pendulum j.

translation of the base mass j, namely x_{b_j}, is ruled by

$$m_b \ddot{x}_{b_j} = -P_j \sin\theta_j - F_{bl_j} - F_{br_j} - F_j \tag{2}$$

in which m is the mass, P_j is the magnitude of the reaction force between the pendulum j and the base mass j, and F_j denotes the active internal force exchanged by the pendulum j and the base mass j along the x-axis: its significance will be clarified in Section III. Also, let c be the damping, k the stiffness, and l_0 the rest length (i.e., the distance between two adjacent base masses when the elastic force is zero); in general, the forces acting on each internal mass of the base because of the adjacent masses are

$$F_{bl_j} = c_b(\dot{x}_{b_j} - \dot{x}_{b_{j-1}}) + k_b(x_{b_j} - x_{b_{j-1}} - l_0) \tag{3a}$$

$$F_{br_j} = c_b(\dot{x}_{b_j} - \dot{x}_{b_{j+1}}) + k_b(x_{b_j} - x_{b_{j+1}} + l_0). \tag{3b}$$

For clarity, F_{bl_j} and F_{br_j} are the left and right forces, respectively. Hence, summing the two members of (3), the overall internal forces of the masses $j = 2, \ldots, n-1$ are

$$F_{b_j} = F_{bl_j} + F_{br_j} = -c_b\,\dot{x}_{b_{j-1}} + 2\,c_b\,\dot{x}_{b_j} - c_b\,\dot{x}_{b_{j+1}} + \\ - k_b\,x_{b_{j-1}} + 2\,k_b\,x_{b_j} - k_b\,x_{b_{j+1}} \tag{4}$$

whereas the actions concerning the end masses are

$$F_{b_1} = c_b\,\dot{x}_{b_1} - c_b\,\dot{x}_{b_2} + k_b\,x_{b_1} - k_b x_{b_2} + k_b l_0 + F_{\text{ext}} \tag{5a}$$

$$F_{b_n} = c_b\,\dot{x}_{b_n} - c_b\,\dot{x}_{b_{n-1}} + k_b\,x_{b_n} - k_b\,x_{b_{n-1}} - k_b l_0 \tag{5b}$$

where $F_{\text{ext}} = c_{\text{ext}}\,\dot{x}_{b_1} + k_{\text{ext}}\,x_{b_1}$ is the force produced by the damper c_{ext} and the spring k_{ext} that connect the end mass to the external world (see Fig. 1): The role of F_{ext} will be clarified in the following.

Deriving (1) twice with respect to time and making use of it, the equations of motion of the pendula are as follows:

$$\begin{aligned} m_p \ddot{x}_{p_j} &= m_p \left[\ddot{x}_{b_j} + l(\ddot{\theta}_j \cos\theta_j - \dot{\theta}_j^2 \sin\theta_j)\right] \\ &= P_j \sin\theta_j + F_j \end{aligned} \tag{6a}$$

$$\begin{aligned} m_p \ddot{y}_{p_j} &= m_p \left[l(\ddot{\theta}_j \sin\theta_j + \dot{\theta}_j^2 \cos\theta_j)\right] \\ &= -P_j \cos\theta_j - m_p g \end{aligned} \tag{6b}$$

where g is the gravitational acceleration.

Some steps allow rearranging (1)–(6) in a system of second-order ordinary differential equations (ODEs) with the form

$$\ddot{\mathbf{x}} = \mathbf{A}^{-1}\mathbf{b} = \begin{bmatrix} \mathbf{A}_{11} & \mathbf{A}_{12} \\ \mathbf{A}_{21} & \mathbf{A}_{22} \end{bmatrix}^{-1} \mathbf{b} \tag{7}$$

where

$$\mathbf{x} = \begin{bmatrix} x_{b_1} & \ldots & x_{b_n} & \theta_1 & \ldots & \theta_n \end{bmatrix}^T \tag{8}$$

$$\mathbf{A}_{11} = \text{diag}(m_b + m_p, \ldots, m_b + m_p)_{n\times n} \tag{9a}$$

$$\mathbf{A}_{12} = \text{diag}(m_p l \cos\theta_1, \ldots, m_p l \cos\theta_n)_{n\times n} \tag{9b}$$

$$\mathbf{A}_{21} = \text{diag}(m_b \cos\theta_1, \ldots, m_b \cos\theta_n)_{n\times n} \tag{9c}$$

$$\mathbf{A}_{22} = \text{diag}(-m_p l(\sin\theta_1)^2, \ldots, -m_p l(\sin\theta_n)^2)_{n\times n} \tag{9d}$$

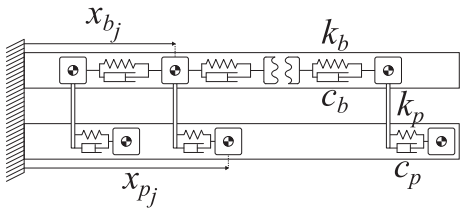

Fig. 2. Schematic of planar linear pendula on flexible base (Model *B*).

$$\mathbf{b} = \begin{bmatrix} m_p l \dot{\theta}_1^2 \sin\theta_1 - F_{b_1} \\ \vdots \\ m_p l \dot{\theta}_n^2 \sin\theta_n - F_{b_n} \\ m_p l \dot{\theta}_1^2 \sin\theta_1 \cos\theta_1 - (F_{b_1} + F_1)\cos\theta_1 + m_p g \sin\theta_1 \\ \vdots \\ m_p l \dot{\theta}_n^2 \sin\theta_n \cos\theta_n - (F_{b_n} + F_n)\cos\theta_n + m_p g \sin\theta_n \end{bmatrix}. \tag{10}$$

B. Planar Pendula on Flexible Base (Model B)

This model can be regarded as a simplified version of the previous one since the swinging pendula are replaced by planar ones, and it is particularly interesting because it is linear. The schematic is displayed in Fig. 2. The equation of horizontal motion of the base body $j = 2, \ldots, n-1$ is

$$\begin{aligned} &m_b \ddot{x}_{b_j} + c_p \dot{x}_{b_j} - c_p \dot{x}_{p_j} + k_p x_{b_j} - k_p x_{p_j} + \\ &- c_b \dot{x}_{b_{j-1}} + 2\, c_b \dot{x}_{b_j} - c_b \dot{x}_{b_{j+1}} + \\ &- k_b x_{b_{j-1}} + 2\, k_b x_{b_j} - k_b x_{b_{j+1}} = 0. \end{aligned} \tag{11}$$

For the leading and trailing masses, the equation simplifies to

$$\begin{aligned} &m_b \ddot{x}_{b_1} + c_p \dot{x}_{b_1} - c_p \dot{x}_{p_1} + k_p x_{b_1} - k_p x_{p_1} \\ &+ c_b \dot{x}_{b_1} - c_b \dot{x}_{b_2} + k_b x_{b_1} - k_b x_{b_2} = 0 \end{aligned} \tag{12a}$$

$$\begin{aligned} &m_b \ddot{x}_{b_n} + c_p \dot{x}_{b_n} - c_p \dot{x}_{p_n} + k_p x_{b_n} - k_p x_{p_n} \\ &+ c_b \dot{x}_{b_n} - c_b \dot{x}_{b_{n-1}} + k_b x_{b_n} - k_b x_{b_{n-1}} = 0 \end{aligned} \tag{12b}$$

where the rest length is set to zero. Furthermore, the dynamics of the linear pendulum j is

$$m_p \ddot{x}_{p_j} - c_p \dot{x}_{b_j} + c_p \dot{x}_{p_j} - k_p x_{b_j} + k_p x_{p_j} = 0. \tag{13}$$

For convenience, the equations of motion can be arranged in matrix form. Specifically, the mass matrix is

$$\mathbf{M} = \mathrm{diag}(m_b, \ldots, m_b, m_p, \ldots, m_p)_{2n \times 2n}. \tag{14}$$

The damping matrix is

$$\mathbf{C} = \mathbf{C}_p + \mathbf{C}_b = \begin{bmatrix} c_p \mathbf{I}_n & -c_p \mathbf{I}_n \\ -c_p \mathbf{I}_n & c_p \mathbf{I}_n \end{bmatrix} + \begin{bmatrix} \mathbf{C}_{b_{11}} & \mathbf{0}_n \\ \mathbf{0}_n & \mathbf{0}_n \end{bmatrix} \tag{15}$$

where $\mathbf{I}_n$ is the n-by-n identity matrix, $\mathbf{0}_n$ is the n-by-n zero matrix, and

$$\mathbf{C}_{b_{11}} = \begin{bmatrix} c_b & -c_b & & & \\ -c_b & 2\,c_b & -c_b & & \\ & \ddots & \ddots & \ddots & \\ & & -c_b & 2\,c_b & -c_b \\ & & & -c_b & c_b \end{bmatrix}. \tag{16}$$

Likewise, the stiffness matrix is

$$\mathbf{K} = \mathbf{K}_p + \mathbf{K}_b = \begin{bmatrix} k_p \mathbf{I}_n & -k_p \mathbf{I}_n \\ -k_p \mathbf{I}_n & k_p \mathbf{I}_n \end{bmatrix} + \begin{bmatrix} \mathbf{K}_{b_{11}} & \mathbf{0}_n \\ \mathbf{0}_n & \mathbf{0}_n \end{bmatrix} \tag{17}$$

in which

$$\mathbf{K}_{b_{11}} = \begin{bmatrix} k_b & -k_b & & & \\ -k_b & 2\,k_b & -k_b & & \\ & \ddots & \ddots & \ddots & \\ & & -k_b & 2\,k_b & -k_b \\ & & & -k_b & k_b \end{bmatrix}. \tag{18}$$

By defining

$$\mathbf{x} = \begin{bmatrix} x_{b_1} & \ldots & x_{b_n} & x_{p_1} & \ldots & x_{p_n} \end{bmatrix}^T \tag{19}$$

the matrix equation of dynamics displays the classic form

$$\mathbf{M}\ddot{\mathbf{x}} + \mathbf{C}\dot{\mathbf{x}} + \mathbf{K}\mathbf{x} = \mathbf{0}. \tag{20}$$

Alternatively, the matrices can be assembled according to the state-space representation

$$\dot{\mathbf{q}} = -\begin{bmatrix} \mathbf{0} & \mathbf{M} \\ \mathbf{M} & \mathbf{C} \end{bmatrix}^{-1} \begin{bmatrix} -\mathbf{M} & \mathbf{0} \\ \mathbf{0} & \mathbf{K} \end{bmatrix} \mathbf{q} = \mathbf{D}\,\mathbf{q} \tag{21}$$

where

$$\mathbf{q} = \begin{bmatrix} \dot{\mathbf{x}}^T & \mathbf{x}^T \end{bmatrix}^T \tag{22}$$

and the resulting matrix $\mathbf{D}$ is the so-called dynamic matrix.

III. Analysis of Parallel Pendula Models

In order to get a first insight of the physics behind the aforementioned experiments about clock and metronome synchronization, it is reasonable to formulate a model, such as Model *A*, *with a large value of base stiffness* ($k_b \to \infty$) because the platform that holds the oscillators is essentially rigid, and pendula have a swinging motion rather than reciprocating. Initially, it is worth setting $F_j = 0$, which means that there is no active force between the base and the pendula. Also, the base is connected to the external world, thanks to the spring with stiffness k_{ext} and to the damper with coefficient c_{ext}: the latter is the only dissipative action (the damping due to c_b is negligible, owing to the assumption that $k_b \to \infty$), so it is the sole contribution that can alter the trajectory of the system, driving it through a less resistive path. In other words, if there is a chance for the pendula to synchronize, this damper (c_{ext}) is entirely responsible for that, which proves the significance of F_{ext} in such a configuration.

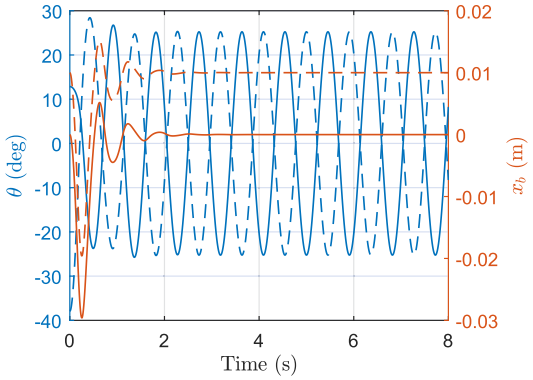

Fig. 3. Simulation of antiphase synchronization of two pendula (solid for $j = 1$ and dashed for $j = 2$). The system is subjected to the external force F_{ext}, and $F_j = 0$. $m_b = 0.5\,\text{kg}$, $m_p = 1\,\text{kg}$, $c_b = 10\,\text{Ns/m}$, $k_b = 1\,\text{GN/m}$ (large value suitable to describe an essentially rigid base), $c_{\text{ext}} = 10\,\text{Ns/m}$, $k_{\text{ext}} = 0\,\text{N/m}$, $l = 0.2\,/\text{m}$, and $l_0 = 1\,\text{cm}$.

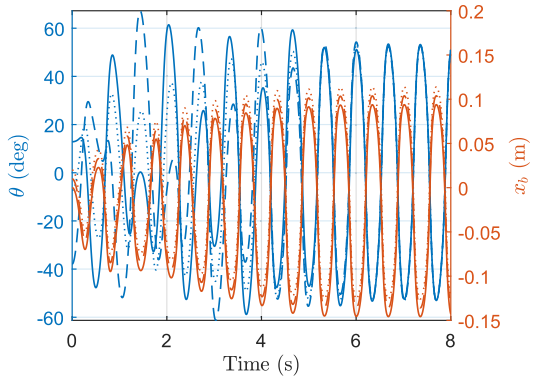

Fig. 4. Simulation of in-phase synchronization of three oscillators. The system is subjected to the van-der-Pol force F_j. $\mu = 0.4\,\text{Ns/m}$ and $\theta_0 = 0.4\,\text{rad}$. $m_b = 0.33\,\text{kg}$, $m_p = 1\,\text{kg}$, $c_b = 10\,\text{Ns/m}$, $k_b = 1\,\text{GN/m}$ (large value suitable to describe an essentially rigid base), $c_{\text{ext}} = 0\,\text{Ns/m}$, $k_{\text{ext}} = 0\,\text{N/m}$, $l = 0.2\,\text{m}$, and $l_0 = 1\,\text{cm}$.

Consequently, it is clear that, as soon as the (rigid) base stops, the pendula will preserve their oscillations perpetually. Based on these consideration, it is easy to realize that, when $n = 2$, the pendula are identical, and c_{ext} is adequate, the two oscillators are prone to achieve antiphase synchronization while the speeds of the two base masses fade to zero (see Fig. 3). Indeed, such a configuration is visibly balanced and allows the system to minimize the power losses. However, when $n > 2$, in-phase or antiphase synchronization becomes unlikely because there is an infinite number of balanced oscillations that ensure the stillness of the base. At this point, the need for an additional term to extend the region of synchronization is clear. Pantaleone [4] proposed a van-der-Pol-like action that reads

$$F_j = \mu \left(1 - \left(\frac{\theta_j}{\theta_0}\right)^2\right) \dot{\theta}_j \tag{23}$$

where μ and θ_0 are the tuning parameters, which is generally adopted to mimic the damping and driving effects of the metronome escapement. In fact, this solicitation introduces energy into the system; therefore, the (in-phase) synchronization can occur regardless of the presence of the external damper. Moreover, the in-phase coordination of all oscillators requires the base to vibrate antiphase with respect to the pendula (see Fig. 4). Fig. 4 also testifies the presence of an active energy supply since the amplitude of all oscillations tends to grow until the equilibrium is attained.

The choice to equip Model *A* with a flexible base originates from the assumption that the synchronization of metronomes observed in the famous experiment is not exclusively related to the escapement, but it mainly descends from the propagation of vibrations along the base by virtue of its intrinsic flexibility. At present, the authors do not know whether the conjecture is correct with respect to metronomes sympathy, but certainly the hypothesis guides to a system with some captivating properties considering its eventual emulation in the electrical domain. Indeed, Model *A with a moderate value of base stiffness* exhibits a notable synchronization potential in the presence of passive elements, which means that there is no need of further external

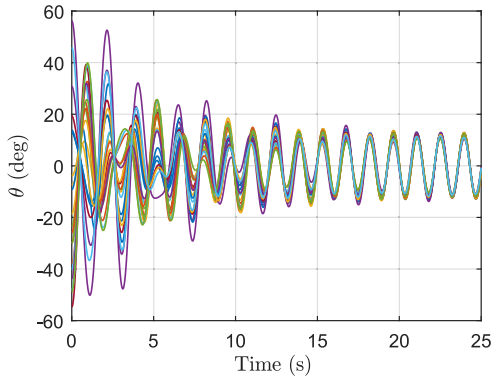

Fig. 5. Simulation of an array of 20 pendula synchronizing when connected to a flexible base. The synchronicity emerges plainly from the chaotic motion at the cost of a given amount of initial energy. $m_b = 1\,\text{kg}$, $m_p = 1\,\text{kg}$, $c_b = 10\,\text{Ns/m}$, $k_b = 10\,\text{N/m}$ (value suitable to describe an essentially flexible base), $c_{\text{ext}} = 0\,\text{Ns/m}$, $k_{\text{ext}} = 0\,\text{N/m}$, and $l = 1\,\text{m}$.

supplies to make any number of pendula oscillate in unison. A graphical demonstration of such capabilities is provided by Fig. 5, which collects the results of an exemplary simulation. Specifically, Fig. 5 depicts the angular positions of an array of 20 pendula across a time span of 25 s. Similarly to what we observed above, the damping plays a fundamental role as it allows the system to approach a synchronous mode of vibration. Indeed, as soon as the synchronicity occurs, the base and the set of pendula behave as two rigid bodies, which implies that the platform does not dissipate energy any more, thanks to the null relative motion of its masses. This aspect is confirmed by the steadiness of the envelopes of pendula oscillations in the presence of synchronicity (see Fig. 5). Naturally, since the system is fully passive, there can be unfavorable initial conditions that cause the system to dissipate a substantial amount of its starting energy during the transient, leading to small oscillations in stationary conditions.

Essentially, the only limitation of Model *A* is its nonlinearity, a drawback overcome by Model *B* while preserving all benefits of its predecessor. Additionally, thanks to its linear form, it

TABLE II
IMPEDANCE ANALOGY: MECHANICAL AND ELECTRICAL EQUIVALENCE

Mechanical		Electrical	
Quantity	Symbol	Quantity	Symbol
Mass	m	Inductance	L
Damping	c	Resistance	R
Stiffness	k	Inverse capacity	$1/C$
Displacement	x	Charge	q

is possible to apply basic modal analysis to further deepen the insight into the natural vibration modes and frequencies of the system [33]. Briefly, defining $\lambda_1, \lambda_2, \ldots, \lambda_j, \ldots, \lambda_{4n}$ the (complex conjugate pairs of) eigenvalues of the dynamic matrix in (21), the damped angular natural frequencies of the system are given by

$$\omega_{d_j} = |\lambda_j| \tag{24}$$

whereas, the relative damping of a given vibration mode, which essentially indicates the likelihood of a certain mode to prevail over the others, is

$$\zeta_j = \frac{\Re(\lambda_j)}{\omega_{d_j}} \tag{25}$$

in which $\Re(\cdot)$ denotes the real part. Moreover, the eigenvectors of the dynamic matrix hold the geometrical properties of such modes in terms of relative vibration amplitudes and phase shifts.

IV. IMPEDANCE ANALOGY

To exploit the features of Model *B* within a power converter, the mechanical system must be translated to the electrical equivalent. To this end, based on the impedance analogy, the correspondence reported in Table II can be established. This parallelism allows rewriting (11)–(13) within the electric domain

$$\begin{aligned} &L_b\ddot{q}_{b_j} + R_p\,\dot{q}_{b_j} - R_p\dot{q}_{p_j} + \frac{1}{C_p}\,q_{b_j} - \frac{1}{C_p}\,q_{p_j} + \\ &- R_b\,\dot{q}_{b_{j-1}} + 2\,R_b\,\dot{q}_{b_j} - R_b\,\dot{q}_{b_{j+1}} + \\ &- \frac{1}{C_b}\,q_{b_{j-1}} + 2\,\frac{1}{C_b}\,q_{b_j} - \frac{1}{C_b}\,q_{b_{j+1}} = 0 \end{aligned} \tag{26}$$

$$\begin{aligned} &L_b\ddot{q}_{b_1} + R_p\,\dot{q}_{b_1} - R_p\dot{q}_{p_1} + \frac{1}{C_p}\,q_{b_1} - \frac{1}{C_p}\,q_{p_1} \\ &+ R_b\,\dot{q}_{b_1} - R_b\,\dot{q}_{b_2} + \frac{1}{C_b}\,q_{b_1} - \frac{1}{C_b}\,q_{b_2} = 0 \end{aligned} \tag{27a}$$

$$\begin{aligned} &L_b\ddot{q}_{b_n} + R_p\,\dot{q}_{b_n} - R_p\dot{q}_{p_n} + \frac{1}{C_p}\,q_{b_n} - \frac{1}{C_p}\,q_{p_n} \\ &+ R_b\,\dot{q}_{b_n} - R_b\,\dot{q}_{b_{n-1}} + \frac{1}{C_b}\,x_{b_n} - \frac{1}{C_b}\,q_{b_{n-1}} = 0 \end{aligned} \tag{27b}$$

$$L_p\ddot{q}_{p_j} - R_p\,\dot{q}_{b_j} + R_p\dot{q}_{p_j} - \frac{1}{C_p}\,q_{b_j} + \frac{1}{C_p}\,q_{p_j} = 0. \tag{28}$$

These ODEs can be further simplified by setting $R_p = 0$ (i.e., $c_p = 0$) and $1/C_b = 0$ (i.e., $k_b = 0$): when the dominant vibration mode takes place, the former condition is essential to make oscillations conservative, the latter is justified by the fact that k_b affects only the transient and it does not contribute to the mode frequency since the base behaves as a single inelastic body.

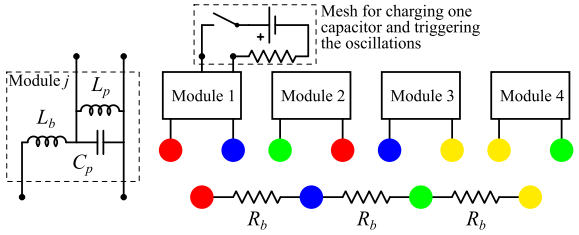

Fig. 6. Schematic of the modular electric circuit. For clarity, four modules are considered, but the scheme can be extended to accommodate any number of units. Dots with matching colors indicate common electrical nodes.

TABLE III
NOMINAL VALUE AND MEASURED RESISTANCE AT 10 kHz OF THE SELECTED COMPONENTS OF THE EXPERIMENTAL CIRCUIT

	L_b	L_p	C_p	R_b
Nominal value	750 µH	250 µH	1.5 µF	100 Ω
Resistance at 10 kHz	≈ 1 Ω	≈ 2 Ω	≈ 10 mΩ	≈ 100 Ω

Equations (26)–(28) correspond to the modular electric circuit, as depicted in Fig 6. The schematic is significant because it may be exploited to synchronize an array of *series-connected* converters, thus maximizing the overall peak voltage [32], [34].

A. Experimental Electrical Setup

To asses the functionality of the proposed self-synchronizing circuit and evaluate its response under real conditions, experimental tests are conducted. Indeed, in actuality, parasitic resistance may alter unfavorably the trajectories, especially due to skin effect when the resonant frequency is high. The relevant system consists of three modules (see Fig. 6) and a switch that permits the charge of one capacitor through a dc power supply: when the switch is engaged, the charge occurs. Subsequently, the switch is opened to trigger the oscillations. The nominal value of the selected components as well as the corresponding resistance at 10 kHz are reported in Table III. Applying (24) and (25), and neglecting the inherent resistance of the components involved, the resonant frequency with null damping is equal to 9490.17 Hz, which also justifies the frequency at which the parasitic resistance is measured (see Table III). The outcome of the experiment is displayed in Fig. 7. When the switch is opened at zero time, the voltage of the capacitor directly connected to the switch starts oscillating, thus dragging also the voltage of the other two. After a short transient, all the signals vibrate in unison and essentially with the same amplitude. As can be inferred from the plot, the resonance occurs at the frequency that can be predicted analytically by modal approach (see Section III). Moreover, since the parasitic resistance is nonnegligible, the

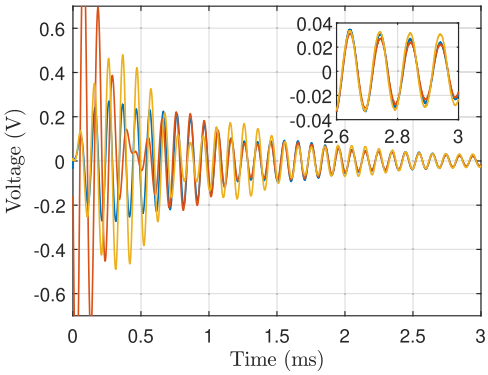

Fig. 7. Experimental test: capacitors voltage during the synchronization transient. Red line corresponds to the capacitor initially charged. The final part is magnified to allow appreciating the sympathy of the oscillators.

TABLE IV
MOBILITY ANALOGY: MECHANICAL AND ELECTRICAL EQUIVALENCE

Mechanical		Electrical	
Quantity	Symbol	Quantity	Symbol
Mass	m	Capacity	C
Damping	c	Conductance	$1/R$
Stiffness	k	Inverse of inductance	$1/L$
Displacement	x	Voltage integral over time	$\int v(t)dt$

response is damped also in the region where the synchronicity subsists.

V. MOBILITY ANALOGY

The mobility analogy represents the dual of the impedance analogy exploited above. Such an approach, which is summarized in Table IV, leads to a system made of *parallel* modules. Indeed, setting $1/R_p = 0$ (i.e., $c_p = 0$) and $1/L_b = 0$ (i.e., $k_b = 0$) based on what stated in Section IV, (11)–(13) can be rewritten as follows in terms of electrical quantities:

$$C_b\dot{v}_{b_j} + \int \frac{v_{b_j} - v_{p_j}}{L_p}dt - \frac{v_{b_{j-1}}}{R_b} + 2\frac{v_{b_j}}{R_b} - \frac{v_{b_{j+1}}}{R_b} = 0 \quad (29)$$

$$C_b\dot{v}_{b_1} + \int \frac{v_{b_1} - v_{p_1}}{L_p}dt + \frac{v_{b_1}}{R_b} - \frac{v_{b_2}}{R_b} = 0 \quad (30a)$$

$$C_b\dot{v}_{b_n} + \int \frac{v_{b_n} - v_{p_n}}{L_p}dt + \frac{v_{b_n}}{R_b} - \frac{v_{b_{n-1}}}{R_b} = 0 \quad (30b)$$

$$C_p\dot{v}_{p_j} - \int \frac{v_{b_j} - v_{p_j}}{L_p}dt = 0. \quad (31)$$

Equations (29)–(30) express the current balance at the nodes where C_b, L_p, and R_b converge. Equation (31) indicates that the current through C_p is the same as the one traversing L_p, i.e., the two components are series connected. Also, by summing up (29)–(31), it can be inferred that all capacitors share a node.

Based on these equations, the circuit, as depicted in Fig. 8, can be derived. It is worth observing that such an arrangement does not reflect faithfully the aforementioned equations because, for

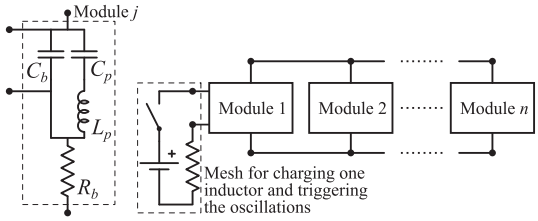

Fig. 8. Schematic of the electric circuit with self-synchronizing parallel-connected modules.

TABLE V
NOMINAL VALUE AND MEASURED RESISTANCE AT 100 Hz OF THE SELECTED COMPONENTS OF THE EXPERIMENTAL CIRCUIT

	L_p	C_b	C_p	R_b
Nominal value	750 µH	195 µF	∞	10 Ω
Resistance at 100 Hz	$\approx$ 40 mΩ	$\approx$ 290 Ω	0 Ω	$\approx$ 10 Ω

symmetry purposes, each module integrates a resistor. In fact, according to (29)–(31), the resistors should be placed between consecutive modules. This modification is possible because it does not alter substantially the response of the circuit as well as its inherent tendency to the synchronicity.

A. Experimental Electrical Setup

Also the passive parallel circuit is validated experimentally by connecting three modules, as indicated in Fig. 8. The nominal values of the selected parameters are listed in Table V, and, based on (24) and (25), they determine a resonant frequency of 415 Hz. The choice to replace C_p with a short circuit (i.e., $C_p = \infty$) does not compromise the synchronization of the system and will be mathematically justified in the rest of the article. Essentially, this modification prevents the average voltage across the entire module from drifting away from zero, which is mandatory for the correct operation of a converter that outputs ac power. The dynamic response of the system is triggered by means of a switch that, when closed, injects some current from a dc power supply through one inductor: as soon as the switch is opened, the inductor current starts oscillating, thus disturbing also the other modules, which start vibrating in turn. The experimental results are condensed in Fig. 9, which depicts the three inductors' currents during the synchronization transient as well as the related phases. In the early stage, the current of the preloaded inductor is the most intense, and it is slightly out of phase compared with the other two, but after ≈ 10 ms, all the inductor currents attain the balancing both in terms of phase and amplitude.

VI. VOLTAGE-SOURCE CONTROLLER DESIGN

In order to take advantage of the topology, as described in Section V, it is possible to develop a distributed controller that manipulates the PWM of each dc/ac power converter to inject a signal that emulates the voltage of the self-synchronizing circuit (depicted in Fig. 8). A similar approach is followed by Johnson et al. [18].

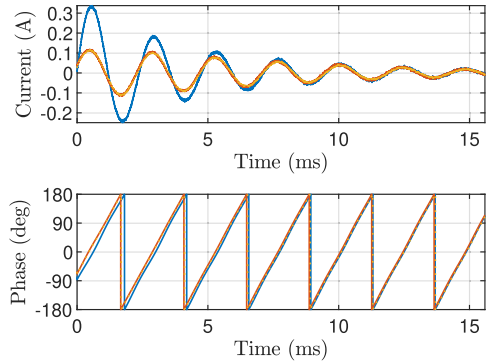

Fig. 9. Experimental test: inductor currents (top) and the corresponding phases (bottom) during the synchronization transient.

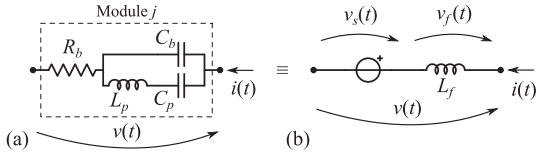

Fig. 10. Equivalence between the (a) module j and (b) voltage source $v_s(t)$ in series with the residual inductance L_f at the working frequency. The overall voltage difference $v(t) = v_s(t) + v_f(t)$ across the branch subject to the current $i(t)$ equals that of the module under the same current. In a real circuit, $v_s(t)$ is the voltage that must be at the terminals of the inverter to emulate the pendulum response.

A. Transfer Function Design

The first step is the derivation of the transfer function

$$H(s) = V_s(s)/I(s) \tag{32}$$

representing the voltage $V_s(s) = \mathcal{L}\{v_s\}(s)$ across a single-inverter per unit current $I(s) = \mathcal{L}\{i\}(s)$ in the Laplace domain, where $\mathcal{L}$ denotes the Laplace transform operator and s is the complex frequency. By applying the Laplace transform to the branches a and b in Fig. 10 and imposing their equality, the following expression of the transfer function is obtained:

$$H_{nc}(s) = \frac{\frac{1}{C_b C_p} + \frac{L_p}{C_b}s^2}{\left(\frac{1}{C_b} + \frac{1}{C_p}\right)s + L_p s^3} + R_b - L_f s. \tag{33}$$

Furthermore, C_p capacitor has a particular effect that requires special attention. As can be inferred from the frequency response of $H_{nc}(s)$ when $L_f = 0$, a finite value of the capacitor can cause the drift of the output voltage. Such an undesired response reflects the presence of a negative slope of $-20\,\mathrm{dB}$ per decade in the leftmost region of the magnitude graph (see Fig. 11). The trend flattens where the first zero, z_0, is located. In addition, the lower the frequency with respect to z_0, the faster the drift. By increasing the C_p value, z_0 tends to move toward the origin so that the limit of z_0 as C_p approaches infinity equals 0. In practical terms, if C_p capacitor is replaced by a short circuit, the output drift is prevented at low frequencies. Fig. 11 illustrates two tunings of $H_{nc}(s)$ exhibiting the resonant frequency at 50 Hz: one (solid line) with $L_f = 0$, $L_p = 100\,\mu\mathrm{H}$, $R_b = 0.1\,\Omega$, $C_b = 131.6\,\mathrm{mF}$, and $C_p = 440.2\,\mathrm{mF}$, and the other (dashed line) with

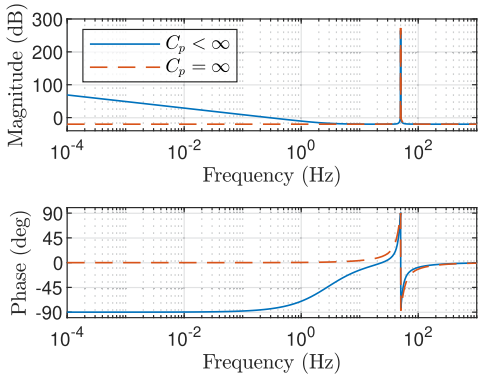

Fig. 11. Bode diagram with magnitude (top) and phase (bottom) of $H_{nc}(s)$ when $L_f = 0$: effect of C_p capacitor. Both parametrizations yield a resonant frequency of 50 Hz.

the same parameters except $C_b = 101.32\,\mathrm{mF}$ and $C_p = \infty$. It is evident that the two characteristics are very similar above $z_0 = 2.81$ Hz, whereas they differ below in terms of both magnitude and phase shift.

Unfortunately, (33) corresponds to a noncausal system, i.e., the number of zeros is higher than the number of poles. To overcome such an issue, the last term can be rewritten with the inclusion of a low-pass filter characterized by a cutoff frequency α, namely

$$H(s) = \frac{\frac{1}{C_b C_p} + \frac{L_p}{C_b}s^2}{\left(\frac{1}{C_b} + \frac{1}{C_p}\right)s + L_p s^3} + R_b - \frac{\alpha L_f s}{\alpha + s}. \tag{34}$$

Further algebraic steps allow expressing (34) in the conventional form $H(s) = N(s)/D(s)$, where

$$\begin{aligned} N(s) = {} & (R_b L_p - \alpha L_f L_p)\, s^4 + \left(R_b L_p \alpha + \frac{L_p}{C_b}\right) s^3 \\ & + \left(\frac{L_p \alpha}{C_b} + \left(\frac{1}{C_b} + \frac{1}{C_p}\right) R_b - \left(\frac{1}{C_b}\frac{1}{C_p}\right) L_f \alpha\right) s^2 \\ & + \left(\frac{1}{C_b C_p} + \left(\frac{1}{C_b} + \frac{1}{C_p}\right) R_b \alpha\right) s + \frac{\alpha}{C_b C_p} \end{aligned} \tag{35}$$

$$D(s) = L_p s^4 + L_p \alpha s^3 + \left(\frac{1}{C_b} + \frac{1}{C_p}\right) s^2 + \left(\frac{1}{C_b} + \frac{1}{C_p}\right) \alpha s. \tag{36}$$

However, owing to the presence of R_b, and because of the parasitic resistance of the circuit, $H(s)$ exhibits a decaying response, which prevents the system from sustaining a constant voltage. In order to compensate the virtual and real losses and, in general, to control the source voltage (or current) amplitude, it is possible to modify the transfer function by computing $V_s(s)$ when the system defined by (32) is subject to the augmented current i_a such that

$$\begin{aligned} \mathcal{L}\{i_a\}(s) &= I_a(s) = I(s) + I_x(s) \\ &= I(s) - G_x V_s(s) = (1 - G_x H(s))\, I(s) \end{aligned} \tag{37}$$

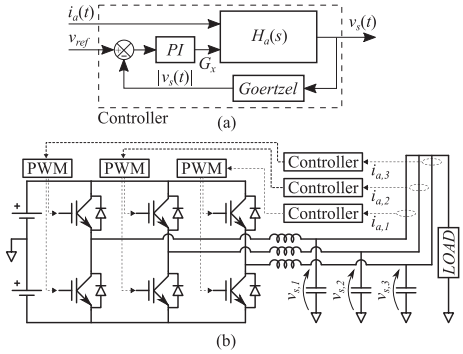

Fig. 12. (a) Structure of the controller. (b) Schematic of the experimental parallel circuit with a three-phase inverter as three single-phase converters. The *LC* filters attenuate the harmonics generated by the switches, leaving the fundamental component untouched.

where the additional current term $I_x(s)$ is defined as a function of the conductance G_x and of $V_s(s)$. From (37), $I(s) = I_a(s)/(1 - G_x H(s))$, which can be plugged in (32): the new transfer function that relates the source voltage and the augmented current is

$$H_a(s) = \frac{V_s(s)}{I_a(s)} = \frac{H(s)}{1 - G_x H(s)} = \frac{N(s)}{D(s) - G_x N(s)}. \quad (38)$$

Hence, the conductance G_x is a control input that can be manipulated to attain the desired voltage amplitude for the power converter by adding ($G_x > 0$) or subtracting ($G_x < 0$) power from the system. For completeness, when $G_x = 0$, i.e., $I_x(s) = 0$, $H_a(s)$ coincides with $H(s)$.

B. Distributed Controller Design and Validation

1) Three-Phase Inverter as Three Single-Phase Converters: The proposed distributed controller is developed upon (38). Specifically, each control unit implements the structure, as depicted in Fig. 12(a): the module processes the current signal $i_a(t)$ provided by Allegro ACS712 sensor, corrects $v_s(t)$ amplitude by PI regulator returnitng G_x, and updates the dynamic response of the transfer function $H_a(s)$ via second-order Runge–Kutta solver. Moreover, Goertzel algorithm is exploited to retrieve the voltage amplitude (i.e., $|v_s(t)|$) to be compared with the desired load voltage v_{ref}. For completeness, in the context of the present study, G_x is regulated based on the voltage amplitude error, but it could be alternatively adjusted according to the current amplitude error; also, v_{ref} is a constant parameter of the controller, and, in general, it is chosen in such a way that it matches the rated voltage of the load.

The validation makes use of a three-phase dc/ac converter (i.e., inverter) whose legs are managed separately in such a way that they act as three distinct single-phase converters. Clearly, this configuration is such that all the three parallel converters share the same dc link (input), which is typical of high-current applications. The inverters are controlled by an STM32 Nucleo–F446RE board. The overall modular circuit comprising the three parallel-connected voltage sources is reported in Fig. 12(b).

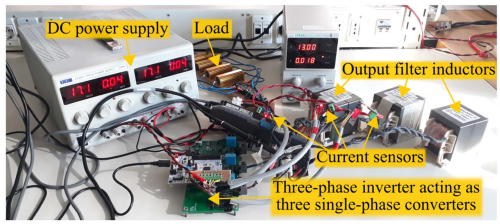

Fig. 13. Photograph of the experimental setup.

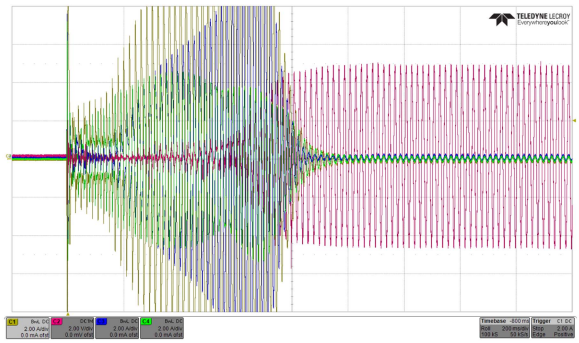

Fig. 14. Experimental results concerning three single-phase converters with the same dc link: load voltage (magenta) and current signals.

Since the voltage signals produced by the inverters are PWM-modulated square waves (bare sinusoidal PWM is adopted), *LC* branches are needed to recover the fundamental components. Finally, a purely resistive load equal to 10 Ω is applied in parallel.

The transfer function is tuned in order to obtain a natural frequency of 50 Hz, namely, $L_p = L_f = 100\,\mu\text{H}$, $C_b = 101.32\,\text{mF}$, C_p is replaced by a short circuit ($C_p = \infty$), $R_b = 0.1\,\Omega$, and $\alpha = 400\,\text{rad/s}$. Fig. 13 reports the actual experimental setup.

The performed experiment consists in forcing the system in a chaotic initial condition: this is achieved by preloading with random numbers the transfer function integrators. The procedure aims at assessing the response of the distributed control under substantial asynchronicity. The outcomes of the test are displayed in Fig. 14, where the three currents and the load voltage are depicted. As the system approaches the synchronous motion, the load voltage moves from a distorted trend to a regular sinusoid with the target amplitude ($v_{\text{ref}} = 5\,\text{V}$). Fig. 15 displays in more detail the three current waveforms. The controller is turned on at zero time. Despite the chaotic transient triggered by the artificial starting condition, the current signals attain the synchronicity in approximately 1 s. Fig. 15 includes also three magnified areas useful to highlight the evolution of the waveforms: initially, the current is distorted and relatively intense due to the circulating fraction (top-left inset) [14]; subsequently, it assumes a decaying sinusoidal shape (top-right inset), and finally, it settles at a sine wave with substantially constant magnitude (bottom-right inset).

2) Single-Phase Inverters With Distinct DC Links: Assessing the functionality of the proposed controller also when the parallel-operating inverters have distinct dc links is paramount

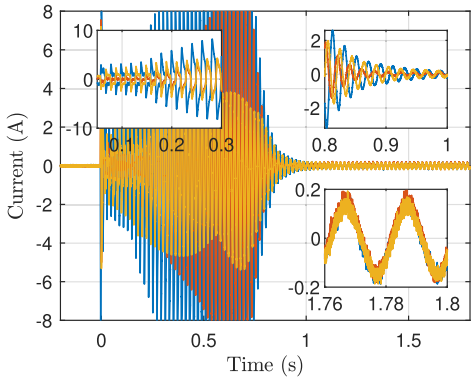

Fig. 15. Current signals of the three modules during the synchronization transient. The magnified areas highlight the evolution of the trend.

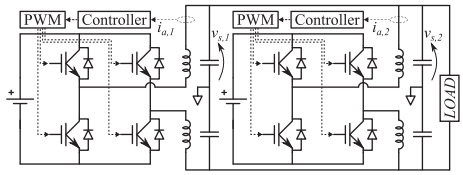

Fig. 16. Schematic of the experimental parallel circuit with two single-phase inverters with distinct dc links. See Fig. 12(a) for the details of the controller.

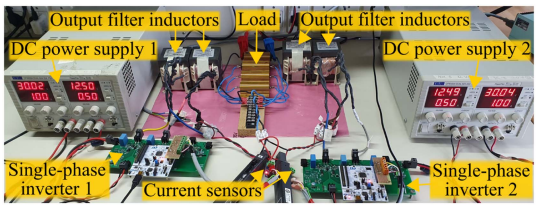

Fig. 17. Photograph of the experimental setup.

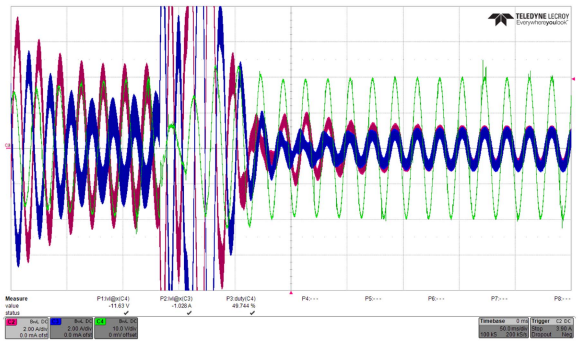

Fig. 18. Experimental results concerning two single-phase inverters with distinct dc links: load voltage (green); and output currents.

because this configuration is typical of some real networks, such as microgrids. Fig. 16 depicts the schematic of two single-phase inverters connected in parallel, which corresponds to the experimental setup, as displayed in Fig. 17.

The outcomes of the experimental test that is carried out are reported in Fig. 18. In particular, the figure shows that the output

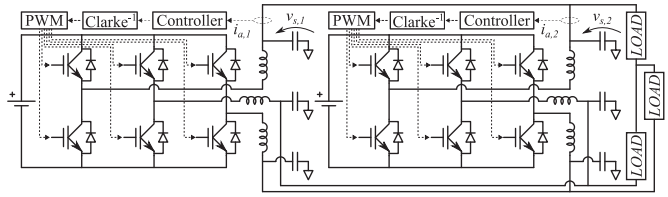

Fig. 19. Schematic of the experimental parallel circuit with two three-phase inverters with distinct dc links. See Fig. 12(a) for the details of the controller. The block "Clarke^{-1}" denotes the inverse Clarke transformation.

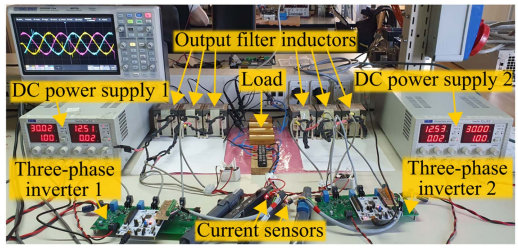

Fig. 20. Photograph of the experimental setup.

currents of the two inverters (blue and magenta waveforms) initially exhibit asynchronous response; anyway, when both controllers are enabled, the in-phase synchronization is quickly attained, and the output voltage (green waveforms) becomes a solid sine wave with the desired frequency and amplitude (in this test, v_{ref} is set to 20 V).

3) Three-Phase Inverters With Distinct DC Links: Since three-phase systems are ubiquitous, it is essential to prove that the proposed controller can also deal with parallel-operating three-phase inverters. By analogy with the previous section is Section VI-B2, Fig. 19 shows the schematic of two three-phase inverters with separate dc links, and Fig. 20 reports the real implementation of such a diagram.

A marginal adaptation is required to interface the controller with three-phase systems: specifically, as in [20], amplitude-preserving forward and inverse Clarke transformations are exploited to switch between abc-frame and $\alpha\beta$-frame. By doing so, the controller can operate as it was connected to a single-phase converter. It is worth pointing out that, since the considered three-phase system is balanced, only the output current of phase a has to be measured, and this coincides with the current of phase α; hence, forward transformation can be omitted. Also, it is worth noting that the inverse transformation is applied to the controller output and to its quadrature component, which can be recovered from the former by a proper filter (such as an all-pass filter).

The experimental results are shown in Figs. 21 and 22. The former testifies the synchronization of the output currents' pairs of two phases, whereas the latter attests the resulting three-phase load voltage waveforms. In this experiment, v_{ref} is set to 10 V. Very similar results are achieved when the two converter units are connected to the same dc link in accordance with the results of Section VI-B1.

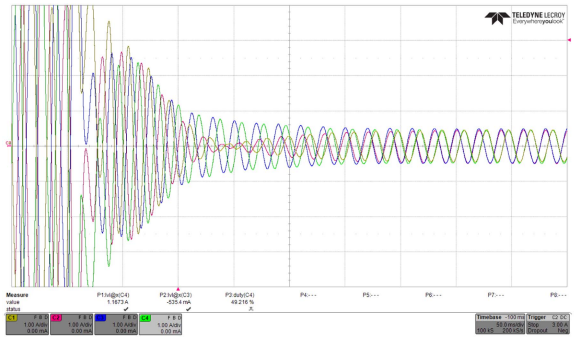

Fig. 21. Experimental results concerning two three-phase inverters with distinct dc links: output currents' pairs of two phases.

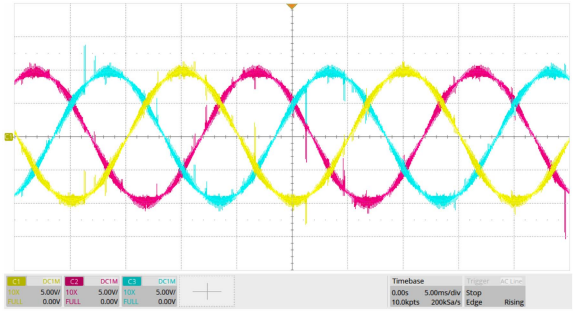

Fig. 22. Experimental results concerning two three-phase inverters with distinct dc links: three-phase load voltages.

VII. Conclusion

This work affirms that it is possible to obtain self-synchronizing circuits by projecting mechanical models with intrinsic sympathy for the synchronicity into the electrical domain. Interestingly, the study proved that the same mechanical model can lead to two substantially different circuits depending on the adopted analogy. The mobility analogy gives rise to a network made of series-connected units, whereas the impedance analogy generates a circuit with parallel modules. The latter topology, as demonstrated by the present investigation, can be emulated within the digital controller of a voltage-source converter, thus obtaining a distributed regulator suitable to synchronize all modules with no need of explicit communication. The mostly linear nature of such a regulator makes its implementation and tuning straightforward. Further research is needed to assess how the controller deals with asymmetric load sharing among the converters, nonlinear loads, and the sudden insertion or removal of units.

Acknowledgment

This work was developed in the facilities of PExLab.

References

[1] M. Bennett, M. F. Schatz, H. Rockwood, and K. Wiesenfeld, "Huygens's clocks," *Proc. Roy. Soc. London. Ser. A, Math., Phys. Eng. Sci.*, vol. 58, no. 2019, Mar. 2002, pp. 563–579.

[2] F. N. Hoogeboom, A. Y. Pogromsky, and H. Nijmeijer, "Huygens' inspired multi-pendulum setups: Experiments and stability analysis," *Chaos, Interdiscipl. J. Nonlinear Sci.*, vol. 26, Nov. 2016, Art. no. 116304.

[3] R. Dilao, "On the problem of synchronization of identical dynamical systems: The Huygens's clocks," Springer New York, vol. 33, pp. 163–181, Jun. 2009.

[4] J. Pantaleone, "Synchronization of metronomes," *Amer. J. Phys.*, vol. 70, no. 10, pp. 992–1000, Oct. 2002.

[5] J. Saha, N. B. Y. Gorla, and S. K. Panda, "Analytical expression-based modulation for soft-switched matrix-based dual-active-bridge (S2MB-DAB) single-phase AC-DC converter," *IEEE J. Emerg. Sel. Topics Power Electron.*, vol. 10, no. 6, pp. 6511–6522, Dec. 2022.

[6] J. Saha, N. B. Y. Gorla, and S. K. Panda, "Implementation of power balance control scheme for a cascaded matrix-based dual-active-bridge (CMB-DAB) MVAC-LVDC converter," *IEEE Trans. Ind. Appl.*, vol. 58, no. 1, pp. 388–399, Jan./Feb. 2022.

[7] J. E. Huber and J. W. Kolar, "Optimum number of cascaded cells for high-power medium-voltage AC–DC converters," *IEEE J. Emerg. Sel. Topics Power Electron.*, vol. 5, no. 1, pp. 213–232, Mar. 2017.

[8] J. E. Huber, J. Böhler, D. Rothmund, and J. W. Kolar, "Analysis and cell-level experimental verification of a 25 kW all-SiC isolated front end 6.6 kV/400 V AC-DC solid-state transformer," *CPSS Trans. Power Electron. Appl.*, vol. 2, no. 2, 140–148 Jun. 2017.

[9] J. Saha, N. Kumar, and S. K. Panda, "A futuristic silicon-carbide (SiC)-based electric-vehicle fast charging/discharging (FC/dC) station," *IEEE J. Emerg. Sel. Topics Power Electron.*, vol. 11, no. 3, pp. 2904–2917, Jun. 2023.

[10] J. Saha and S. K. Panda, "Overview and comparative analysis of bidirectional cascaded modular isolated medium-voltage AC–low-voltage DC (MVAC-LVDC) power conversion for renewable energy rich microgrids," *Renewable Sustain. Energy Rev.*, vol. 174, Mar. 2023, Art. no. 113118.

[11] J. E. Huber and J. W. Kolar, "Solid-state transformers: On the origins and evolution of key concepts," *IEEE Ind. Electron. Mag.*, vol. 10, no. 3, pp. 19–28, Sep. 2016.

[12] D. Richards, "A new concept in modular motor drive systems," in *Proc. IEEE 5th Eur. Conf. Power Electron. Appl.*, 1993, pp. 179–181.

[13] E. K. Sato and A. Kawamura, "Decentralized control for redundant parallelism of uninterruptible power supplies with different ratings using only current sensors," in *Proc. IEEE 36th Conf. Power Electron. Specialists Conf.*, 2005, pp. 2823–2829.

[14] A. Soldati, V. Undre, C. Concari, B. A. Alsayid, and M. H. Dradi, "Parallel operation of voltage source converters without filter inductors: Control of the circulating current," in *Proc. IEEE 2nd Int. Conf. Ind. Electron. Sustain. Energy Syst.*. Cagliari, Italy, 2020, pp. 125–130.

[15] J. Rocabert, A. Luna, F. Blaabjerg, and P. Rodrïguez, "Control of power converters in AC microgrids," *IEEE Trans. Power Electron.*, vol. 27, no. 11, pp. 4734–4749, Nov. 2012.

[16] K. De Brabandere, B. Bolsens, J. van den Keybus, A. Woyte, J. Driesen, and R. Belmans, "A voltage and frequency droop control method for parallel inverters," *IEEE Trans. Power Electron.*, vol. 22, no. 4, pp. 1107–1115, Jul. 2007.

[17] Y. Guan, J. M. Guerrero, X. Zhao, J. C. Vasquez, and X. Guo, "A new way of controlling parallel-connected inverters by using synchronous-reference-frame virtual impedance loop-Part I: Control principle," *IEEE Trans. Power Electron.*, vol. 31, no. 6, pp. 4576–4593, Jun. 2016.

[18] B. B. Johnson, S. V. Dhople, A. O. Hamadeh, and P. T. Krein, "Synchronization of parallel single-phase inverters with virtual oscillator control," *IEEE Trans. Power Electron.*, vol. 29, no. 11, pp. 6124–6138, Nov. 2014.

[19] B. B. Johnson, S. V. Dhople, A. O. Hamadeh, and P. T. Krein, "Synchronization of nonlinear oscillators in an LTI electrical power network," *IEEE Trans. Circuits Syst. I, Reg. Papers*, vol. 61, no. 3, pp. 834–844, Mar. 2014.

[20] B. B. Johnson, S. V. Dhople, J. L. Cale, A. O. Hamadeh, and P. T. Krein, "Oscillator-based inverter control for islanded three-phase microgrids," *IEEE J. Photovolt.*, vol. 4, no. 1, pp. 387–395, Jan. 2014.

[21] B. B. Johnson, M. Sinha, N. G. Ainsworth, F. Dorfler, and S. V. Dhople, "Synthesizing virtual oscillators to control islanded inverters," *IEEE Trans. Power Electron.*, vol. 31, no. 8, pp. 6002–6015, Aug. 2016.

[22] B. Johnson, M. Rodriguez, M. Sinha, and S. Dhople, "Comparison of virtual oscillator and droop control," in *Proc. IEEE 18th Workshop Control Model. Power Electron.*, Stanford, CA, USA, 2017, pp. 1–6.

[23] M. Sinha, S. Dhople, B. Johnson, N. Ainsworth, and F. Dorfler, "Nonlinear supersets to droop control," in *Proc. IEEE 16th Workshop Control Model. Power Electron.*, Vancouver, BC, Canada,2015, pp. 1–6.

[24] M. Lu, S. Dutta, V. Purba, S. Dhople, and B. Johnson, "A grid-compatible virtual oscillator controller: Analysis and design," in *Proc. IEEE Energy Convers. Congr. Expo.*, Baltimore, MD, USA, 2019, pp. 2643–2649.

[25] M. Li, Y. Gui, Y. Guan, J. Matas, J. M. Guerrero, and J. C. Vasquez, "Inverter parallelization for an islanded microgrid using the Hopf oscillator controller approach with self-synchronization capabilities," *IEEE Trans. Ind. Electron.*, vol. 68, no. 11, pp. 10879–10889, Nov. 2021.
[26] A. Pollakis, L. Wetzel, D. J. Jörg, W. Rave, G. Fettweis, and F. Jülicher, "Synchronization in networks of mutually delay-coupled phase-locked loops," *New J. Phys.*, vol. 16, no. 11, Nov. 2014.
[27] F. Dorfler and F. Bullo, "Synchronization and transient stability in power networks and non-uniform Kuramoto oscillators," in *Proc. Amer. Control Conf.*. Baltimore, MD, USA, 2010, pp. 930–937.
[28] J. W. Simpson-Porco, F. Dörfler, and F. Bullo, "Synchronization and power sharing for droop-controlled inverters in islanded microgrids," *Automatica*, vol. 49, no. 9, pp. 2603–2611, Sep. 2013.
[29] Y. Kuramoto, "Self-entrainment of a population of coupled non-linear oscillators," in *Proc. Int. Symp. Math. Problems Theor. Phys.*, New York, NY, USA, Springer, 1975.
[30] G.-S. Seo, M. Colombino, I. Subotic, B. Johnson, D. Gros, and F. Dorfler, "Dispatchable virtual oscillator control for decentralized inverter-dominated power systems: Analysis and experiments," in *Proc. IEEE Appl. Power Electron. Conf. Expo.*, Anaheim, CA, USA, 2019, pp. 561–566.
[31] M. Colombino, D. Groz, J.-S. Brouillon, and F. Dorfler, "Global phase and magnitude synchronization of coupled oscillators with application to the control of grid-forming power inverters," *IEEE Trans. Autom. Control*, vol. 64, no. 11, pp. 4496–4511, Nov. 2019.
[32] P. Achanta, M. Sinha, B. Johnson, S. Dhople, and D. Maksimovic, "Self-synchronizing series-connected inverters," in *Proc. IEEE 19th Workshop Control Model. Power Electron.*, Padua, Italy, 2018, pp. 1–6.
[33] A. Brandt, *Noise and Vibration Analysis: Signal Analysis and Experimental Procedures*. Chichester, U.K.: Wiley, 2011.
[34] P. Liu, Z. Chao, and S. Duan, "A digital interconnected bus providing voltage synchronization for the modular series-connected inverters," *IEEE Trans. Power Electron.*, vol. 35, no. 12, pp. 12590–12594, Dec. 2020.

Matteo Dalboni received the M.Sc. degree in mechanical engineering and the Ph.D. degree in information technology from the University of Parma, Parma, Italy, in 2017 and 2021, respectively.

He is currently a Research Assistant with Power Electronics Group, University of Parma. His research interests include vehicle dynamics and control (with focus on fully electric vehicles with independent drives and multiple actuations), and control of power electronics' converters.

Alessandro Soldati (Member, IEEE) received the M.Sc. degree in electronic engineering and the Ph.D. degree in information technology from the University of Parma, Parma, Italy, in 2014 and 2018, respectively. He is a Researcher with the University of Parma, Parma, Italy, in the fields of power electronics and energy engineering. In 2017, he cofounded the spin-off company eDriveLAB for vehicle electrification and was a Visiting Scholar with Aalborg University, Aalborg, Denmark. In 2018, he discussed the Ph.D. thesis about an innovative gate driver that can boost lifetime of power electronics' devices. He was the Principal Investigator of a project funded by Interreg ADRION. He is author of 38 scientific peer-reviewed papers and coinventor of six granted patents.